



Partial Report

## **Brillouin Interaction in Microcavities: Effect of Alumina Layer in the Acoustic Modes of Silica Microspheres**

Letícia de Sousa Magalhães  
Advisor: Gustavo Silva Wiederhecker

Research Field: 10501002 - General Physics  
Admission date: August 2019  
Scholarship: FAPESP  
Process: 2019/14370-0  
Duration: 08/01/2019 to 07/31/2021  
Keywords: *Nonlinear Optics, Scattering, Photonics*

## Chapter 1

### Project Proposal Summary

Brillouin Scattering is a nonlinear interaction responsible for the inelastic scattering of photons mediated by acoustic phonons in transparent media [1], causing energy exchange between the optical and acoustic domains. Because of it, research in SBS has historically aimed at suppressing or accommodating the resulting pump depletion in optical communication systems (as illustrated in fig. 1.1) [2]. It wasn't until last decade's advances in nanofabrication that SBS started to be appreciated as one of the most versatile nonlinear optical effects. The design flexibility of nanophotonics allowed harnessing [3,4], suppressing [5], and tailoring SBS in this platform [6], giving rise to applications such as: narrow-linewidth tunable sources [7–9], all-optical signal processing [10, 11], slow and fast light [12], optical isolation [13], and sensors [14]. In fact, the range of SBS applications is only as limited as our ability to engineer the photon-phonon coupling parameters.

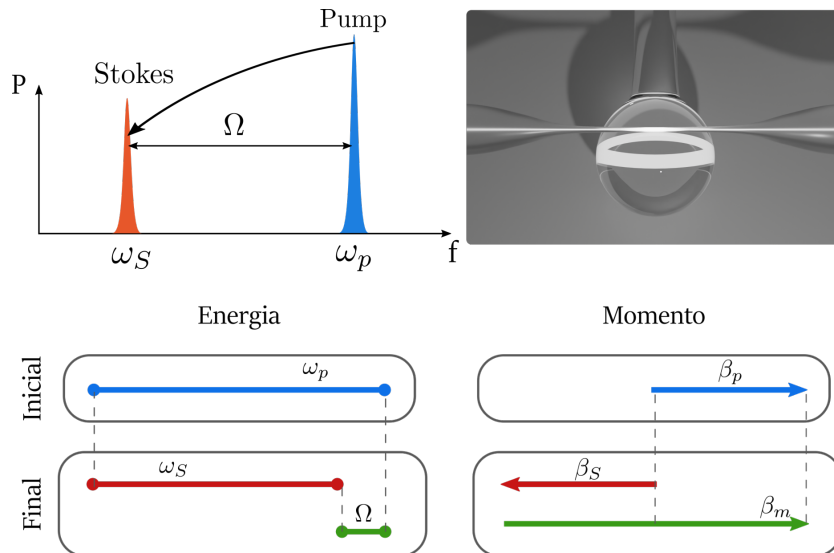


Fig. 1.1: Top left: illustration of pump depletion at fixed Brillouin frequency determined by the mediation phonon. Top right: illustration of coupled light into a silica microsphere. Bottom: phase-matching conditions derived from energy and momentum conservation. Source: Author.

To this end, this project focuses on exploring hybrid material interfaces as an additional degree of freedom to tailor SBS interaction. The chosen platform was silica microspheres encased by alumina thin films. By adding a soft-hard material interface, the spatial distributions for acoustic Rayleigh modes undergo an important transition in character: a surface acoustic wave for thin alumina layers evolves to a bulk-like mode profile in silica for thick films. As illustrated in fig. 1.2, for intermediate values, we theoretically and numerically predict a pseudo-bulk regime where the maximum displacement of the acoustic mode is still at the surface but with greater penetration depth into the sphere. In principle, this provides a mean to co-localize optical and

surface-acoustic modes, a necessary condition to enhance Brillouin interaction.

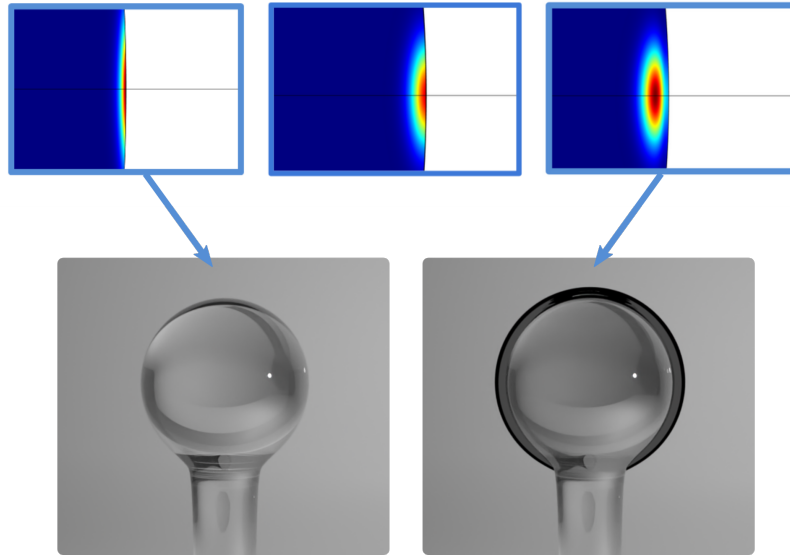


Fig. 1.2: Top: Norm of acoustic mode displacement map for thick (arbitrarily thin) alumina layer in the right (left). Alumina thicknesses from left to right: 0 nm, 50 nm, 500 nm. Pseudo-bulk Rayleigh mode in the middle appears for intermediate thicknesses. Bottom: artistic representation of uncoated (left) and coated (right) samples. Source: Author.

Due to the sophisticated features of the photon-phonon coupling, we stress that co-localization is not a sufficient condition as different coupling mechanisms (photoelastic and moving boundary) could cancel out in non-intuitive ways [5]. Accordingly, an important feature of this project is the theoretical and numerical description of the acoustic modal content in onion-like systems with radially piece-wise uniform mechanical properties. Hence, we can set the following objectives:

1. Experimental characterization of uncoated silica microspheres;
2. Analytical study of elastic wave solution in spherical systems;
3. Numerical implementation of Finite Element Method strategies to obtain fast and accurate acoustic dispersion maps in onion-like systems;
4. Implementation of faster Brillouin gain calculations based on Finite Element Method results;
5. Investigation and design of onion-like geometry responsible for giant Brillouin gain;
6. Experimental investigation of pseudo-bulk acoustic modes via Brillouin scattering interaction.

Thus far, tasks 1,2 and 3 are complete and task 4 is ongoing. It is worth noting that we have readjusted the objectives to accomodate social-distancing guidelines due to the COVID-19 pandemic, ergo the focus on analytical and numerical goals rather than the original intent of an experimentally oriented project. Task 6 is postponed until access to laboratories at UNICAMP is allowed.

## Chapter 2

### Experimental Characterization of Brillouin Scattering in Uncoated Silica Microspheres

During the first semester of this project, an experimental characterization of SBS in uncoated silica microspheres was made. Besides providing the student with an understanding of the samples' spectral characteristics, the task intended the following goals:

- (i) Become acquainted with measurement procedures;
- (ii) Become proficient on analysing the experimental results (software, calibration, code);
- (iii) Map scattering for a trial sample;
- (iv) Automate data acquisition and analysis.

Figure 2.1 shows a schematic of the experimental setup designed to measure backward Brillouin Scattering. In this configuration the laser input wavelength is scanned and a precise calibration is obtained with the top branch, cross-referencing the Mach Zehnder Interferometer signal with the absorption lines in a hydrogen cyanide gas cell (HCN). The signal is statically amplified and any dynamic changes in input power is controlled by an attenuator ( $\text{Att}_{\text{in}}$ ). Next, light is evanescently coupled to the microsphere where we measure: transmitted power, reflected power and reflected spectra. This allows us to track evidence of inelastic scattering and its linearity/nonlinearity with respect to the input power.

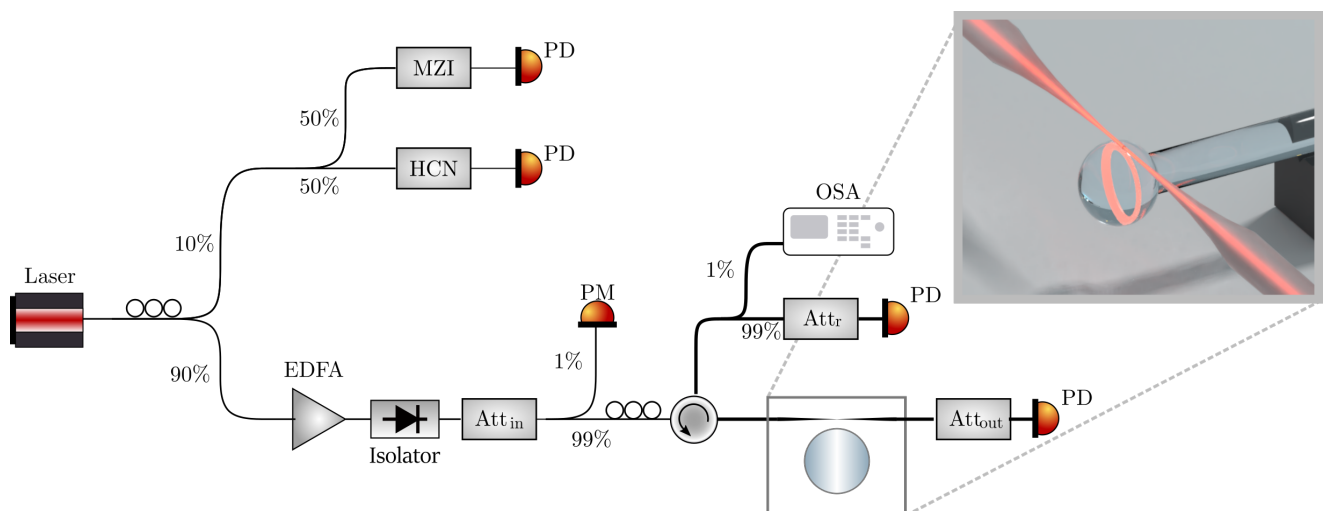


Fig. 2.1: Schematic of the experimental setup. MZI, mach-zehnder interferometer; PM, power meter; PD, photodetector; EDFA, erbium-doped fiber amplifier; Att, attenuator; OSA, optical spectrum analyser; HCN, hydrogen cyanide gas cell. Inset: illustration of taper coupling. Source:Author.

Figure 2.2 shows a measurement of transmission and reflection (signals from the photodetectors after  $\text{Att}_r$  and  $\text{Att}_{\text{out}}$ ) for a 180  $\mu\text{m}$  diameter sphere. We observe a growth in reflection peaks for higher power, being an evidence of a nonlinear back-scattering process. Additionally, for higher powers we observe bistability in the transmitted resonances. Besides shifting the resonances to higher wavelengths, the bistability is responsible for interesting features appearing in the reflected signal. For example, in the 10.5 dBm spectrum near 1559.195 nm there is an intense reflected signal just as the laser leaves a resonance. To adequately investigate these features and confirm the Brillouin nature, we then measured the reflected spectra with the Optical Spectrum Analyser.

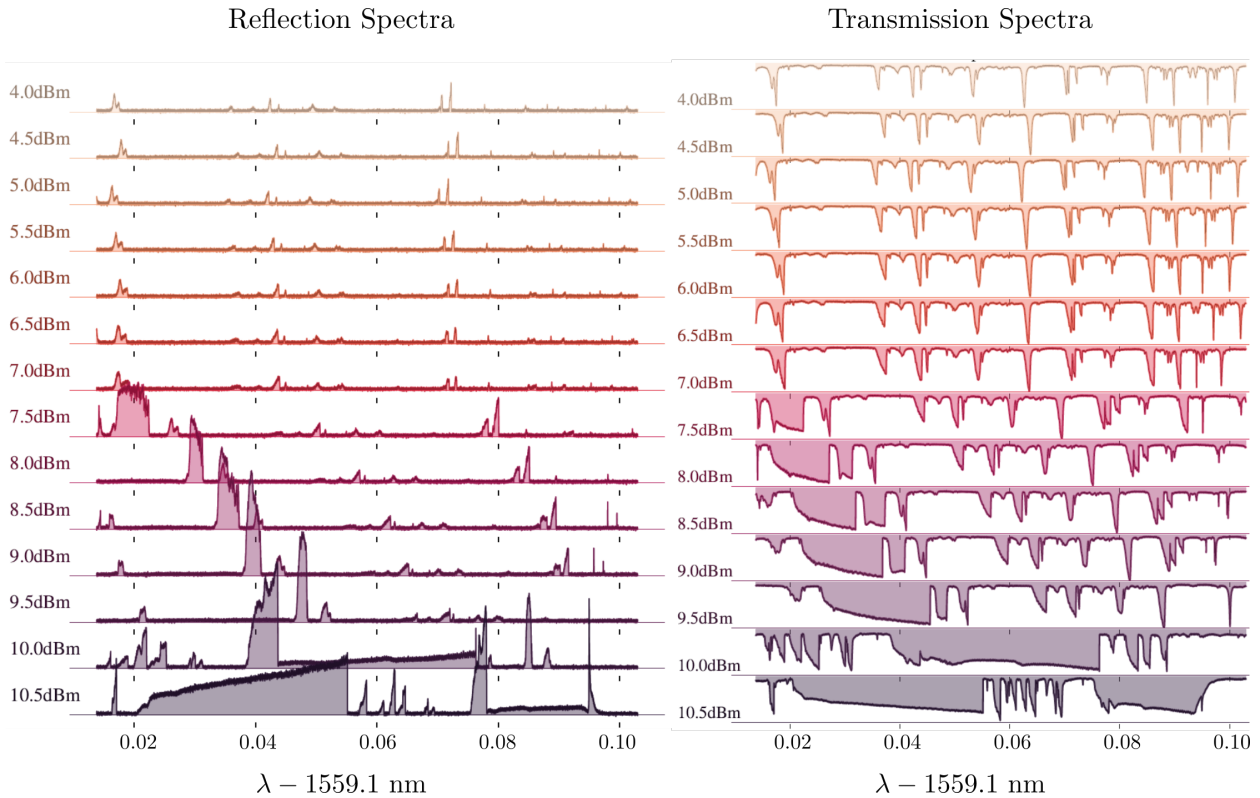


Fig. 2.2: Reflection (left) and transmission (right) spectra for a 180  $\mu\text{m}$  diameter sphere for different input powers. The reflection spectra are normalized according to the input power, thus linear reflection is represented as peaks with equal heights. For high power, thermal bistability is observed.

Figure 2.3 shows the measured spectra varying the input wavelength. We see the presence of inelastic scattering evidence for several input wavelengths. It is also important to notice that a high reflectance signal is not always accompanied by a spectral downshifted Stokes signal, which would be a confirmation of SBS.. Moreover, we analysed the occurrence of frequency-shifted peaks in fig. 2.4. Most scattering events indicate a phonon frequency around 11 GHz, the bulk frequency for a longitudinal wave in silica. As we will show in further sections, the surface acoustic wave has a lower frequency in the 6 GHz range, corresponding to only 0.5% of the scattering events measured. It is worth noting that these measurements correspond to a relatively small sphere, where it is harder to simultaneously satisfy phase-matching and resonance conditions in 6 GHz. Therefore, we expect to see more scattering in the low frequency range for larger samples.

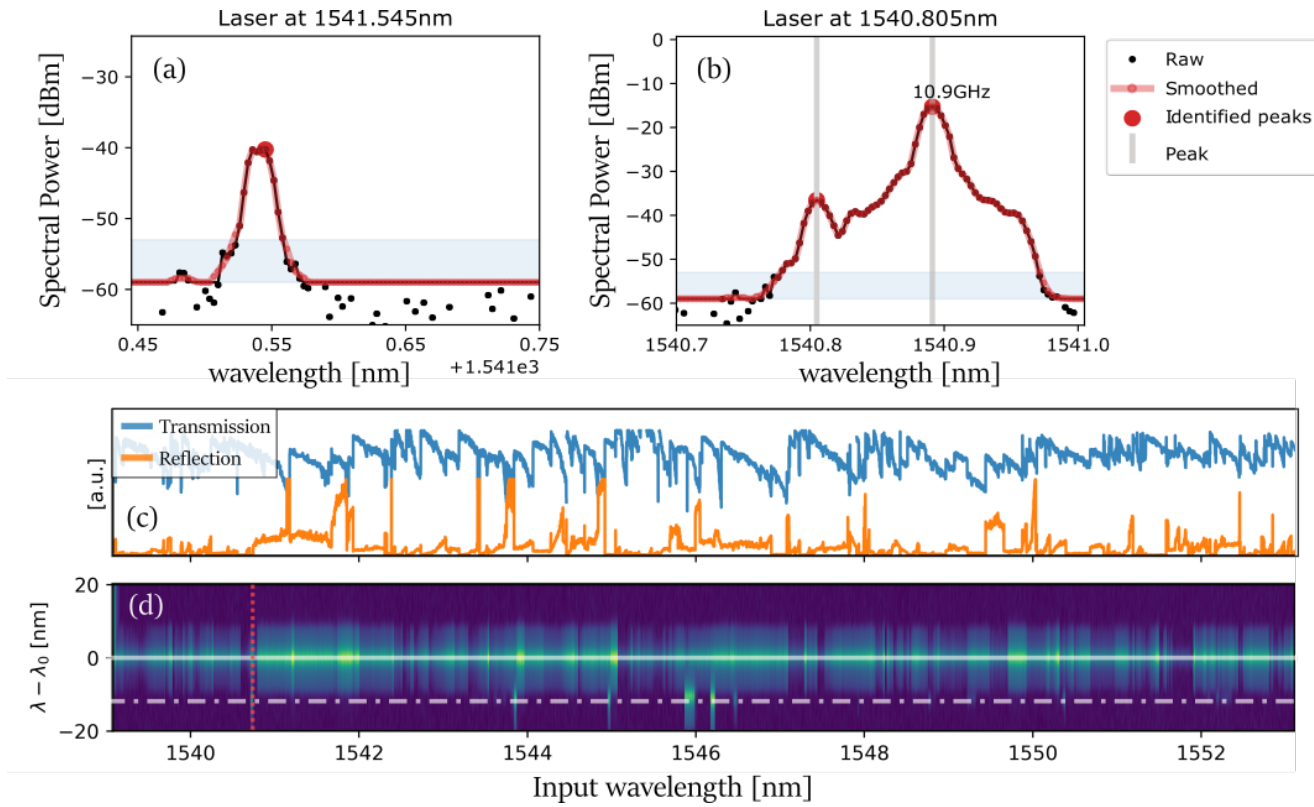


Fig. 2.3: (a, b) Reflected spectra at 1541.545 nm (a) and 1540.805 nm (b) excitation wavelengths. For 1541.545 nm only the linear reflection caused by Rayleigh scattering of the input laser is seen. For 1540.805 nm a second peak appear with 10.9 GHz frequency shift, this is a signature of the inelastic scattering in a Brillouin process. We illustrate the raw data, smoothed set and the identified peaks. (b) Transmission and reflection signals measured with the photodetectors after  $\text{Att}_r$  and  $\text{Att}_{\text{out}}$ . Solid line represents the laser linear reflection, dot-dashed line represents Brillouin shifted peaks and red dotted line represents the spectrum shown in (b). (d) Colormap generated from the collected spectra showing that several input wavelengths display Brillouin peaks.

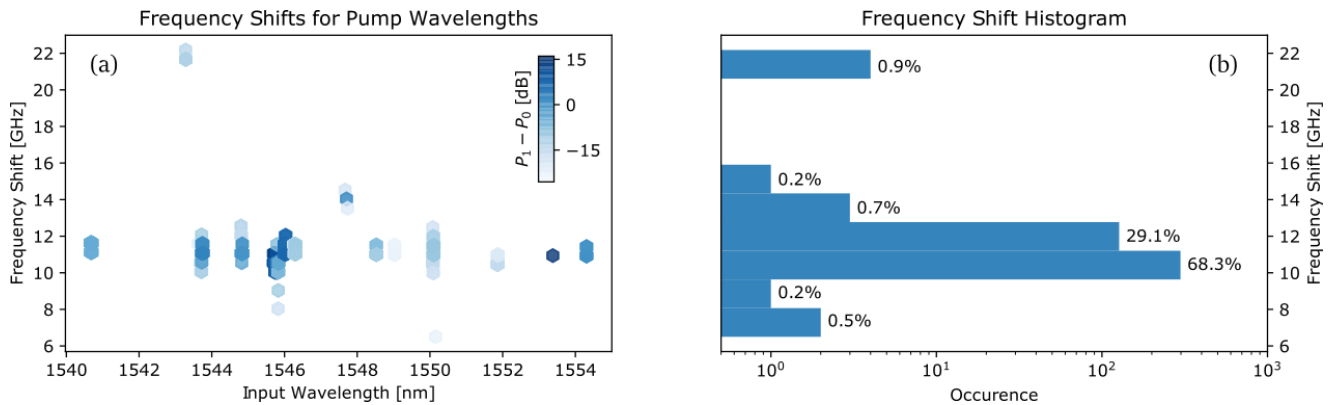


Fig. 2.4: Left: occurrence of frequency shifted peaks as a function of input wavelength. The color scheme indicates the spectral power difference between the scattered peak ,  $P_1$ , and the laser peak,  $P_0$ . Right: histogram showing the occurrence frequency shifts in the entire measurement.

## Chapter 3

### Solution of Free-Vibrational Modes of Elastic Sphere

Understanding Brillouin scattering in a bare silica or coated microsphere requires a detailed comprehension of the acoustic eigenmodes of a spherically symmetric geometry. With that in mind, the original goals for the theoretical portion of this project were:

- (i) Solve dispersion relation for uncoated sphere;
- (ii) Write numerical solution for dispersion of coated sphere and validate results;
- (iii) Simulate coated sphere.

All items above were carried out and the results will be discussed in this chapter. We first present an analytical solution to the problem. As it turns out, the analytical expression is computationally costly to evaluate in the range of interest. Consequently, we reduced the 3D problem to 1D, such that the partial differential equations associated with this problem can be cast into a form that is compatible with an efficient finite element method solution.

### 1 Analytical Solution

We are interested in investigating the case of elastic vibrations in spherically isotropic media. Thus, we begin by considering the elastic wave equation in spherical coordinates.

$$\rho \ddot{\mathbf{u}} = (\lambda + 2\mu) \nabla(\nabla \cdot \mathbf{u}) - \mu \nabla \times (\nabla \times \mathbf{u}), \quad (3.1)$$

where  $\lambda$  and  $\mu$  are the Lame constants,  $\rho$  the medium's density and  $\mathbf{u}$  the mechanical displacement [15, 16]. If we first use the basis of vector spherical harmonics (VSH), eq. (3.2), we are able to express the  $\mathbf{u}$  components only in terms of the radial coordinate. Figures A.1, A.2 and A.3 show a vector representation of the VSH.

$$\begin{aligned} \hat{e}_1 &= \mathbf{Y}_{l,m} = Y_l^m(\theta, \phi) \hat{r} \\ \hat{e}_2 &= r \nabla Y_l^m(\theta, \phi) = \frac{\partial Y_l^m}{\partial \theta} \hat{\theta} + \frac{1}{\sin \theta} \frac{\partial Y_l^m}{\partial \phi} \hat{\phi} \\ \hat{e}_3 &= \mathbf{r} \times \nabla Y_l^m = \frac{1}{\sin \theta} \frac{\partial Y_l^m}{\partial \phi} \hat{\theta} - \frac{\partial Y_l^m}{\partial \theta} \hat{\phi}, \end{aligned} \quad (3.2)$$

with  $-\ell \leq m \leq \ell$  and  $Y_\ell^m(\theta, \phi)$  are the usual scalar spherical harmonic. Defining the longitudinal ( $q$ ) and transverse wavenumbers ( $Q$ )  $q = \sqrt{\frac{\rho}{\lambda+2\mu}} \omega$  and  $Q = \sqrt{\frac{\rho}{\mu}} \omega$ , where  $\omega$  is the angular frequency, the general solution is obtained for the components  $u_1, u_2$

and  $u_3$ :

$$\begin{aligned} u_1 &= \frac{1}{r} \{A_1 [\ell j_\ell(qr) - qr j_{\ell+1}(qr)] + B_1 [\ell(\ell+1) j_\ell(Qr)] + A_2 [\ell y_\ell(qr) - qry_{\ell+1}(qr)] + B_2 [\ell(\ell+1) y_\ell(Qr)]\} e^{-i\omega t} \\ u_2 &= \frac{1}{r} \{A_1 j_\ell(qr) + B_1 [(\ell+1) j_\ell(Qr) - Qr j_{\ell+1}(Qr)] + A_2 y_\ell(qr) + B_2 [(\ell+1) y_\ell(Qr) - Qry_{\ell+1}(Qr)]\} e^{-i\omega t} \\ u_3 &= \{C_1 j_\ell(Qr) + C_2 y_\ell(Qr)\} e^{-i\omega t} \end{aligned} \quad (3.3)$$

where  $j_\ell$  and  $y_\ell$  are Bessel functions of first and second kind and  $A$ ,  $B$  and  $C$  are constant coefficients. It should be noted that inside the sphere only the Bessel functions of first kind exist as the solution cannot diverge at the origin. Therefore  $A_2$ ,  $B_2$  and  $C_2$  must be zero in regions containing the origin.

The respective traction components are:

$$\begin{aligned} F_1 &= \frac{2\mu}{r^2} \{A_1[(\ell^2 - \ell - Q^2 r^2/2)j_\ell(qr) + 2qr j_{\ell+1}(qr)] + B_1 \ell(\ell+1)[(\ell-1)j_\ell(Qr) - Qr j_{\ell+1}(Qr)] + \\ &\quad A_2[(\ell^2 - \ell - Q^2 r^2/2)y_\ell(qr) + 2qry_{\ell+1}(qr)] + B_2 \ell(\ell+1)[(\ell-1)y_\ell(Qr) - Qry_{\ell+1}(Qr)]\} \\ F_2 &= \frac{2\mu}{r^2} \{A_1[(\ell-1)j_\ell(qr) - qr j_{\ell+1}(qr)] + B_1[(\ell^2 - 1 - Q^2 r^2/2)j_\ell(Qr) + Qr j_{\ell+1}(Qr)] + \\ &\quad A_2[(\ell-1)y_\ell(qr) - qry_{\ell+1}(qr)] + B_2[(\ell^2 - 1 - Q^2 r^2/2)y_\ell(Qr) + Qry_{\ell+1}(Qr)]\} \\ F_3 &= \frac{\mu}{r} \{C_1[(\ell-1)j_\ell(Qr) - Qr j_{\ell+1}(Qr)] + C_2[(\ell-1)y_\ell(Qr) - Qry_{\ell+1}(Qr)]\}. \end{aligned} \quad (3.4)$$

At the external surface, the free boundary condition establishes that  $\mathbf{F} = 0$ . Additionally, for an interface between two materials,  $\mathbf{u}$  and  $\mathbf{F}$  must be continuous. Solutions were sought for two special cases: a solid sphere and a layered sphere, i.e., an isotropic sphere encased by a layer of distinct material.

### 1.1 Isotropic Sphere

Consider the case of a solid sphere of radius  $R$ . By setting the free boundary condition we have three equations ( $F_1, F_2, F_3|_{r=R} = 0$ ) and three unknowns ( $A_1, B_1, C_1$ ). Thus, one can express this system of equations by:

$$M \begin{pmatrix} A_1 \\ B_1 \\ C_1 \end{pmatrix} = \begin{pmatrix} 0 \\ 0 \\ 0 \end{pmatrix}, \quad (3.5)$$

$$M = \begin{pmatrix} \frac{(2(\ell-1)\ell - R^2 Q_{in}^2)j_\ell(Rq_{in}) + 4Rq_{in}j_{\ell+1}(Rq_{in})}{R^2} & \frac{2\ell(\ell+1)((\ell-1)j_\ell(RQ_{in}) - RQ_{in}j_{\ell+1}(RQ_{in}))}{R^2} & 0 \\ \frac{2((\ell-1)j_\ell(Rq_{in}) - Rq_{in}j_{\ell+1}(Rq_{in}))}{R^2} & \frac{2\left(-\frac{1}{2}R^2 Q_{in}^2 + \ell^2 - 1\right)j_\ell(RQ_{in}) + RQ_{in}j_{\ell+1}(RQ_{in})}{R^2} & 0 \\ 0 & 0 & \frac{(\ell-1)}{R}j_\ell(RQ_{in}) - Q_{in}j_{\ell+1}(RQ_{in}) \end{pmatrix}. \quad (3.6)$$

Nontrivial solutions appear if the determinant of  $M$  is zero. Therefore, the eigenfrequencies are  $\omega$  such that  $\det(M) = 0$ .

It is worth noting that the basis element  $\hat{e}_3$  can only correspond to torsion without expansion. As  $u_3$  shares no common coefficients with the remainders, it will lead to the so-called for *Torsional modes*, in contrast to *Spheroidal modes* that produce dilatation in addition to torsion. Equation (3.6) highlights in green (red) the torsional (spheroidal) block. Figure 3.1 shows the vectorial displacement character of both families with  $\ell = m$  and fig. 3.2 shows the normalized eigenfrequencies calculated as  $\det(M)$  roots.

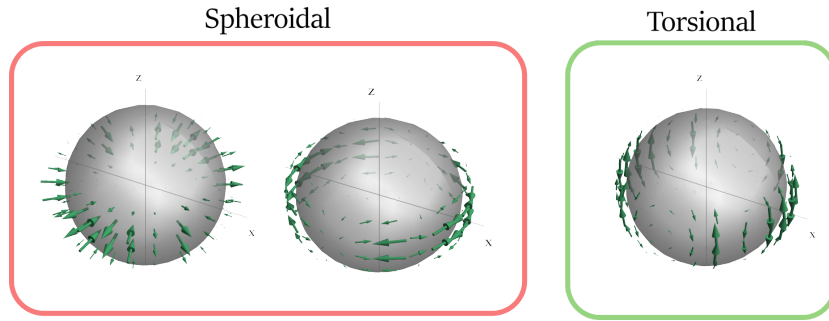


Fig. 3.1: Vectorial character of both families of acoustic modes: spheroidal and torsional. This representation corresponds to  $\ell = m = 15$ .

In fig. 3.2 we also illustrate the different velocity lines: longitudinal, transverse and Rayleigh. Modes above the longitudinal line will induce displacements in the propagation (azimuthal) direction, being a characteristic of pressure acoustic waves. Conversely, modes below the longitudinal line will exhibit stronger displacements in the transverse directions (polar and radial). Lastly we can highlight the first spheroidal mode that lays below the transverse velocity line. This mode asymptotically approaches the Rayleigh velocity line, and is concentrated at the surface thus being called a surface-acoustic mode.

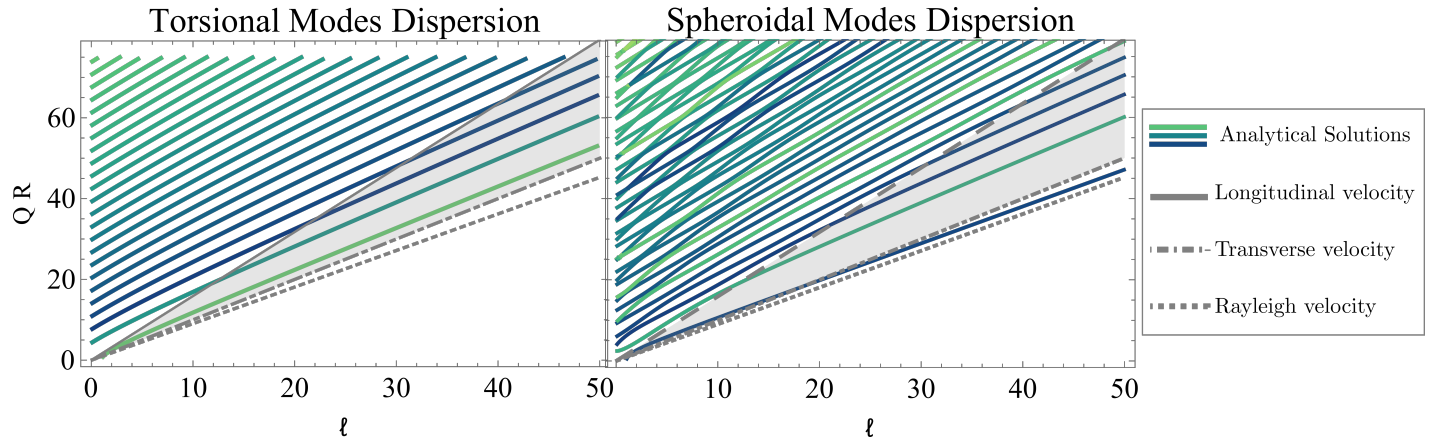


Fig. 3.2: Normalized vibration eigenfrequencies for an elastic sphere as a function of polar angle  $\ell$ . Colored curves represent the roots of the analytical expression (given by equation 3.6) sought by Newton method. We also indicate the correspondent velocity lines for bulk silica: the sound cone between the longitudinal and transverse velocities and the Rayleigh velocity line.

## 1.2 Layered Sphere

Now we assume a sphere with inner radius  $R_0$  encased by a spherical layer of thickness  $t$ . In this situation, the solution discussed for the isotropic sphere is valid for the region containing the origin ( $r < R_0$ ) with unknowns  $(A_1, B_1, C_1)$ . On the other hand, for  $R_0 < r < R_0 + t$  both first and second kind Bessel functions apply. Thus, the solution for the shell comprises six other unknowns  $(A_2, B_2, C_2)$  and  $(A_3, B_3, C_3)$ . Therefore, to determine the total of nine unknowns, three boundary conditions are required, each yielding three equations:

1. Displacement continuity at inner boundary

$$\mathbf{u}(A_1, B_1, C_1) = \mathbf{u}(A_2, B_2, C_2, A_3, B_3, C_3), \text{ at } r = R_0$$

2. Traction continuity at inner boundary

$$\mathbf{F}(A_1, B_1, C_1) = \mathbf{F}(A_2, B_2, C_2, A_3, B_3, C_3), \text{ at } r = R_0$$

3. Free boundary at  $r = R + t$

$$\mathbf{F}(A_2, B_2, C_2, A_3, B_3, C_3) = 0, \text{ at } r = R_0 + t.$$

The matrix equivalent to eq. (3.6) is now  $9 \times 9$  instead of  $3 \times 3$ , with its elements being lengthy combinations of spherical Bessel functions. Figure 3.3 shows the analytical solution for a  $125 \mu\text{m}$  radius sphere and a alumina thickness of 250.

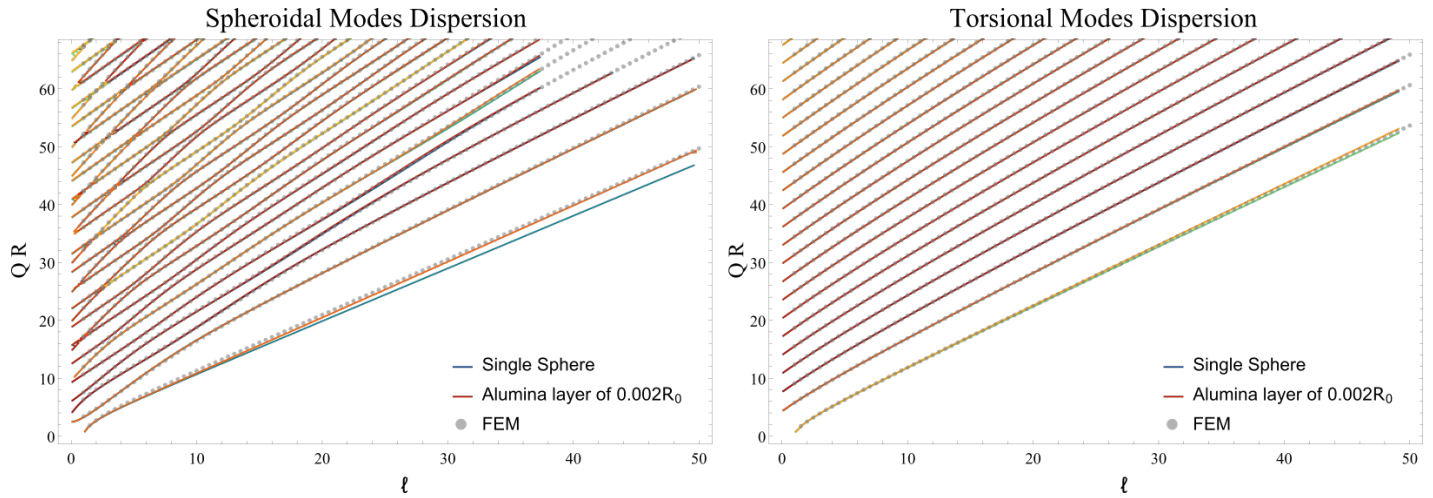


Fig. 3.3: Vibration eigenfrequencies for an elastic sphere (blue curves) and sphere encased by an alumina film with thickness  $0.002R_0$  (red curves). For a  $250 \mu\text{m}$  diameter sphere, this represents a film 500 nm thick film. The gray dots correspond to the Finite Element Method implemented from the weak-form equation for the same encased sphere.

## 2 Numerical Solution by FEM

For Brillouin backscattering in our typical samples with the optical modes with wavelengths around 1550, the phase-matched azimuthal number is around  $m = 1500$ . Considering the fundamental acoustic mode, that implies that  $\ell = m = 1500$  and both layered and single sphere analytical expressions become challenging to calculate numerically. The reason being that the evaluation of Bessel functions of large orders become notoriously costly and unstable due to its oscillatory character, despite having a power series expansion that is everywhere convergent [17, 18]. In fact, to generate the dispersion curves for the spheroidal modes from analytical expression in fig. 3.3, it took 1076.4 s, or 19 min, for the single sphere and 10 987.6 s, or 3 h, for the layered case. The simulations were carried out on a six core Intel Core™ i7-8700 CPU with 24GB RAM.

Consequently, it is of utmost importance to significantly scale up our ability to solve the problem of acoustic dispersion in spherical systems. Ergo, we developed a solution based on a commercial Finite Element Method (FEM) software, reducing the dimension of eq. (3.1) by applying appropriate ansatze for polar and azimuthal contributions.

## 2.1 Separation of variables

To that end, we must first adequately separate the wave equation (eq. (3.1)) [19]. Defining the variables  $U$ ,  $V$  and  $W$ , the  $\mathbf{u}$  components can be expressed as:

$$\begin{aligned} u_r &= W R_0 \\ u_\theta &= \left( -\frac{1}{\sin\theta} \frac{\partial U}{\partial\phi} - \frac{\partial V}{\partial\theta} \right) R_0 \\ u_\phi &= \left( \frac{\partial U}{\partial\theta} - \frac{1}{\sin\theta} \frac{\partial V}{\partial\phi} \right) R_0. \end{aligned} \quad (3.7)$$

Moreover, from spherical symmetry one can assume the ansatz for the angular dependences:

$$\begin{aligned} U &= U_\ell(r) P_\ell^m(\cos\theta) \exp(im\phi) \exp(i\omega t) \\ V &= V_\ell(r) P_\ell^m(\cos\theta) \exp(im\phi) \exp(i\omega t) \\ W &= W_\ell(r) P_\ell^m(\cos\theta) \exp(im\phi) \exp(i\omega t), \end{aligned} \quad (3.8)$$

where  $P_\ell^m(z)$  is the modified Legendre polynomial,  $\ell$  and  $m$  are integers and  $U_\ell$ ,  $V_\ell$  and  $W_\ell$  are the sought radial contributions associated with a polar dependence  $\ell$ .

Defining the dimensionless variables:

$$\begin{aligned} \xi &= R/R_0, \quad \Omega = \omega R_0/v_2, \\ f_1 &= c_{11}/c_{44}, \quad f_2 = c_{12}/c_{44}, \quad f_3 = c_{13}/c_{44}, \quad f_4 = c_{33}/c_{44}, \\ p_1 &= [2(f_3 - f_1 - f_2) - n(n+1)]/f_4, \quad p_2 = -n(n+1)(f_3 + 1)/f_4, \\ p_3 &= n(n+1)(f_1 + f_2 + 1 - f_3)/f_4, \quad p_4 = f_1 - f_2 - n(n+1)f_1 - 2, \\ p_5 &= f_3 + 1, \quad p_6 = f_1 + f_2 + 2. \end{aligned} \quad (3.9)$$

The wave equation then becomes the system of differential equations:

$$\begin{aligned} \xi^2 U_\ell'' + 2\xi U_\ell' + \Omega^2 \xi^2 - [2 + (n^2 + n - 2)(f_1 - f_2)/2] U_\ell &= 0 \\ \xi^2 W_\ell'' + 2\xi W_\ell' + \left( \frac{\Omega^2 \xi^2}{f_4} + p_1 \right) W_\ell - p_2 \xi V_\ell' - p_3 V_\ell &= 0 \\ \xi^2 V_\ell'' + 2\xi V_\ell' + (\Omega^2 \xi^2 + p_4) V_\ell - p_5 W_\ell' - p_6 W_\ell &= 0, \end{aligned} \quad (3.10)$$

and the boundary conditions become:

$$\begin{aligned} \frac{2W_\ell}{\xi} + \frac{n(n+1)V_\ell}{\xi} + \frac{f_4}{f_3} W_\ell' &= 0 \\ \frac{W_\ell}{\xi} + \frac{V_\ell}{\xi} - V_\ell' &= 0 \\ \mu \left( U_\ell' + \frac{U_\ell}{\xi} \right) &= 0. \end{aligned} \quad (3.11)$$

With eq. (3.10) and eq. (3.11) in hand, we can implement the weak-form in the commercial software COMSOL™.

## 2.2 Weak-form - Garlekins' Method

From a FEM perspective, the sought functions are piece-wise defined in a mesh as a combination of basis functions  $\{v\}$  [20,21]. To illustrate the method to obtain a weak-form for a differential equation, consider  $U_\ell$  as sought approximate solutions for equation 3.10. Since  $U_\ell$  is a numerical approximation to the actual solution, one can define the residual  $\varepsilon$  as:

$$\varepsilon = \xi^2 U_\ell'' + 2\xi U_\ell' + \{\Omega^2 \xi^2 - [2 + (n^2 + n - 2)(f_1 - f_2)/2]\} U_\ell \approx 0$$

The best approximation will be the one that reduces  $\varepsilon$  to the least values at all points in the domain. More precisely, the best solution will reduce  $\varepsilon$  in the subspace defined by the basis  $\{v\}$ , this leads to the condition that  $\varepsilon$  has to be orthogonal to the elements  $v$ :

$$\mathcal{R} = \int v \cdot \varepsilon \, d\Omega = 0.$$

Using the chain rule and integrating by parts the first two terms, we get:

$$\begin{aligned} \mathcal{R} &= \int v (\xi^2 U_\ell'' + 2\xi U_\ell' + \{\Omega^2 \xi^2 - [2 + (n^2 + n - 2)(f_1 - f_2)/2]\} U_\ell) \, d\Omega = \\ &= \int v \frac{d}{d\xi} (\xi^2 U_\ell') \, d\xi + \int v \{\Omega^2 \xi^2 - [2 + (n^2 + n - 2)(f_1 - f_2)/2]\} U_\ell \, d\xi = \\ &= - \int \frac{dv}{d\xi} \xi^2 U_\ell' + v \{\Omega^2 \xi^2 - [2 + (n^2 + n - 2)(f_1 - f_2)/2]\} U_\ell \, d\xi = 0. \end{aligned}$$

In particular, the last step is true if the integrand is identically zero, and that is the weak-form equation to be implemented in COMSOL™ in the *PDE interfaces* module. The validation is shown in fig. 3.3 for a layered sphere with layer thickness of  $0.002R_0$  and the results match adequately.

## 2.3 Numerical Results

With this implementation, we are able to solve the acoustic dispersion relations for silica spheres coated with alumina films up to  $10^3$  polar orders. Figure 3.4 shows de dispersion diagrams for different alumina thicknesses. The vertical axis is expressed as  $QR/\ell$ , a normalized phase velocity. For the case of plain silica, at  $\ell = 1400$  the first solution is 6.07 GHz and the second is at 6.91 GHz. We see that the first mode phase velocity increases with layer thickness, eventually crossing the transverse velocity line. Accordingly, fig. 3.5 shows that the surface mode undergoes a transition in character as the film thickness increases. If for a bare sphere its maximum was fixed at the boundary, for 70 nm its maximum is localized 1 μm inside the silica sphere.

This effect can be understood as a perturbation of the Rayleigh wave solution when adding a thin film to a substrate. In our system the substrate, silica, has a transverse sound velocity of 3763 m/s and the substrate, alumina, has an estimated transverse velocity of 8433 m/s. Ergo, for sufficiently thin layers, the high-velocity film will perturb the surface-wave that, in counterpart, will sense a “stiffened” material, thus, increasing the phase-velocity. In the limit of thick layers, the film will constrain the otherwise free surface. One interpretation is that the thick and stiff material will fix the boundary forcing the mode to travel inside the softer substrate. This can be seen in the dispersion curves in fig. 3.5 for a 500 nm layer where the first mode approaches the set of bulk-modes for a bare sphere. Since the family of torsional modes does not comprise any surface-mode, the dispersion diagram shows a slight increase in frequency from 50 nm to 500 nm and no substantial change in mode distribution. The dispersion diagram for

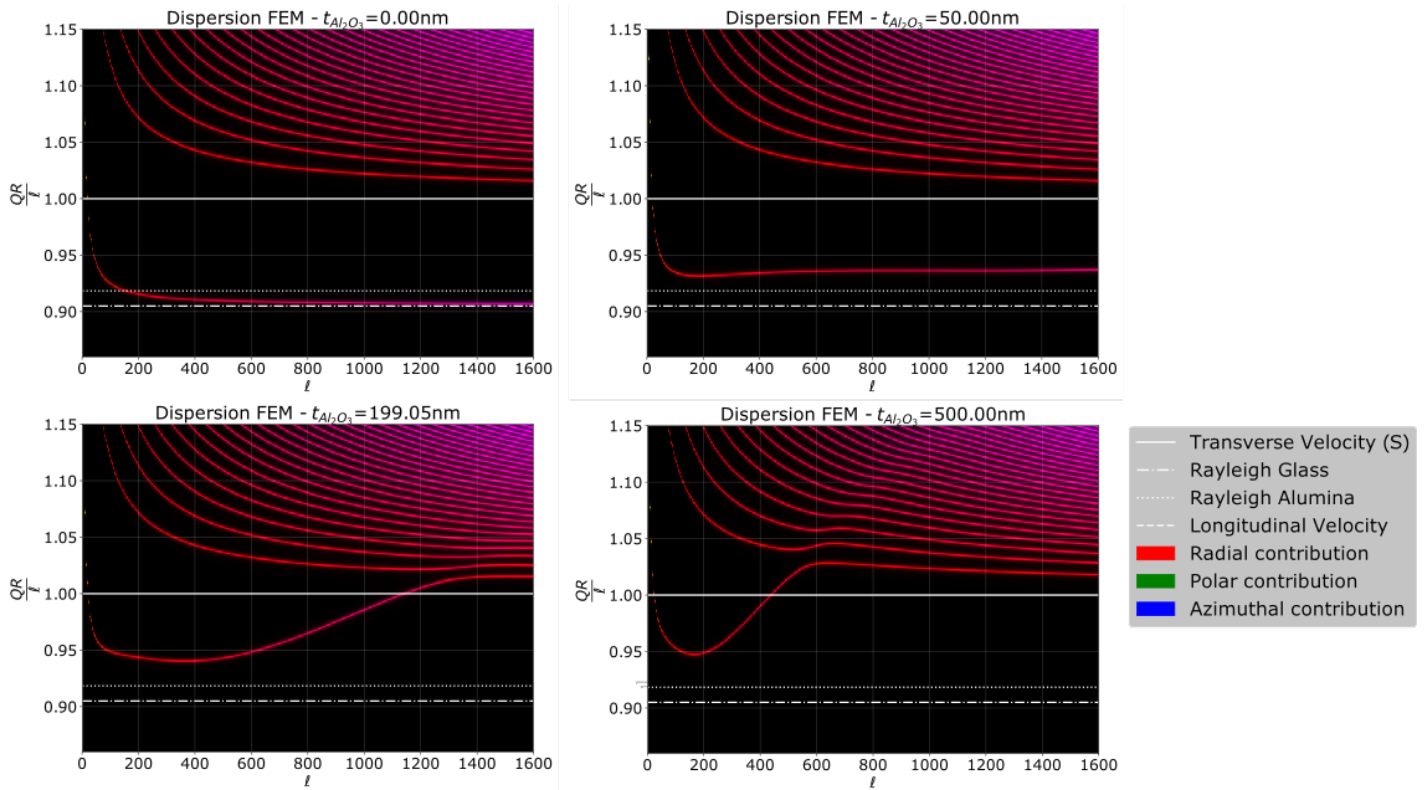


Fig. 3.4: Dispersion diagrams for spheroidal modes obtained by the 1-D weak-form implementation in COMSOL™. The vertical axis corresponds to the normalized phase velocities. Using the silica parameters: Poisson ratio  $\nu_{\text{glass}} = 0.17$ , density  $\rho_{\text{glass}} = 2203 \text{ kg/m}^3$ , Young modulus  $Y_{\text{glass}} = 73 \text{ GPa}$ ; we find that  $\frac{QR}{\ell} = A$  converts to frequency as  $f = A \times \ell \times (4.8 \text{ MHz})$ .

torsional modes is shown in fig. 3.6.

### 3 Evaluation Time Comparison

In contrast to the FEM procedure, we can solve the analytical expression roots using the built-in function `FindRoot` in Mathematica™. This function will numerically search for roots with Newton methods [22]. Here, we consider a sphere with  $250 \mu\text{m}$  diameter and 50 nm alumina layer. For comparison, fig. 3.7 shows the solutions obtained with both analytical and FEM implementation in the range  $1000 \leq \ell \leq 2000$  and we can see a reasonable match. We recorded the time each method took to evaluate the solutions for each polar number. For the analytical approach, the average evaluation time was 175 s, whereas for the FEM solution it was 3.2 s. This represents a 48 times reduction in evaluation time.

On the other hand, analytical expressions for the spheroidal modes are significantly more complex as they derive from a  $6 \times 6$  determinant, in contrast to a  $3 \times 3$  determinant for the torsional modes. For that reason, the `FindRoot` function becomes increasingly costly to evaluate for polar orders higher than 50. Nonetheless, from fig. 3.8 we see that both methods match satisfactorily for low orders. In this case, the average evaluation time for the analytical procedure is 4.2 s and for FEM is 2.2 s.

For higher orders, a precision warning is raised when the function is evaluated (??). If we attempt to search the roots, even with a good initial guess, the method fails to converge to the FEM values despite of increasing evaluation time. This behavior illustrates

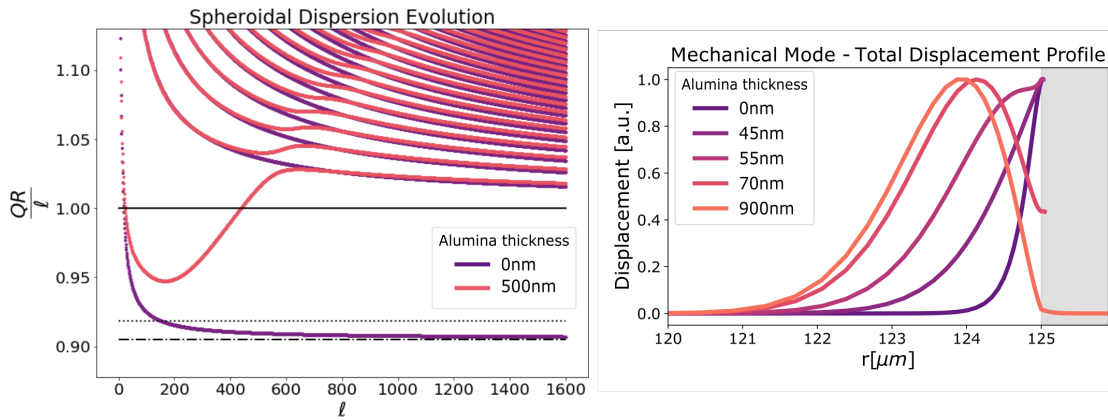


Fig. 3.5: Spherical mode de-localization with respect to added alumina layers. Notice that for 70 nm and 900 nm films the profiles inside the sphere are very similar.

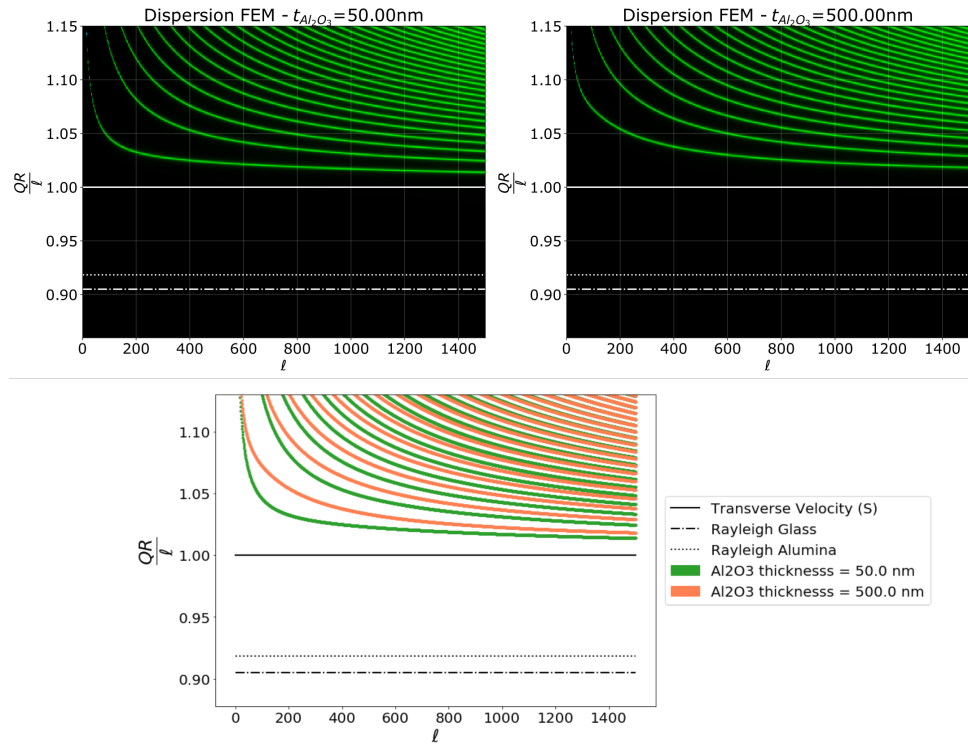


Fig. 3.6: Dispersion diagrams for torsional modes obtained by the 1-D weak-form implementation in COMSOL™. Using the silica parameters: Poisson ratio  $\nu_{\text{glass}} = 0.17$ , density  $\rho_{\text{glass}} = 2203 \text{ kg/m}^3$ , Young modulus  $Y_{\text{glass}} = 73 \text{ GPa}$ ; we find that  $\frac{Q\bar{R}}{\ell} = A$  converts to frequency as  $f = A \times \ell \times (4.8 \text{ MHz})$ .

the paramount necessity of implementing the 1-D weak-form of the elastic wave equation in spherical coordinates.

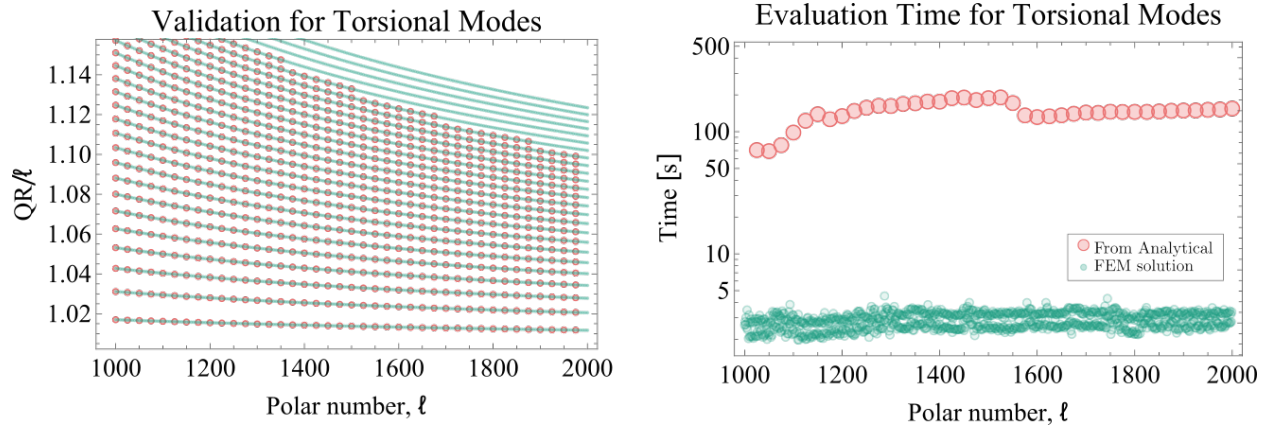


Fig. 3.7: Evaluation time comparison for torsional modes for a sphere with  $250\text{ }\mu\text{m}$  diameter and 50 nm alumina layer. Left: Comparison between results obtained from FEM approach and from numerically solving the dispersion equation  $\det(M) = 0$ . Right: evaluation time comparison for both procedures.

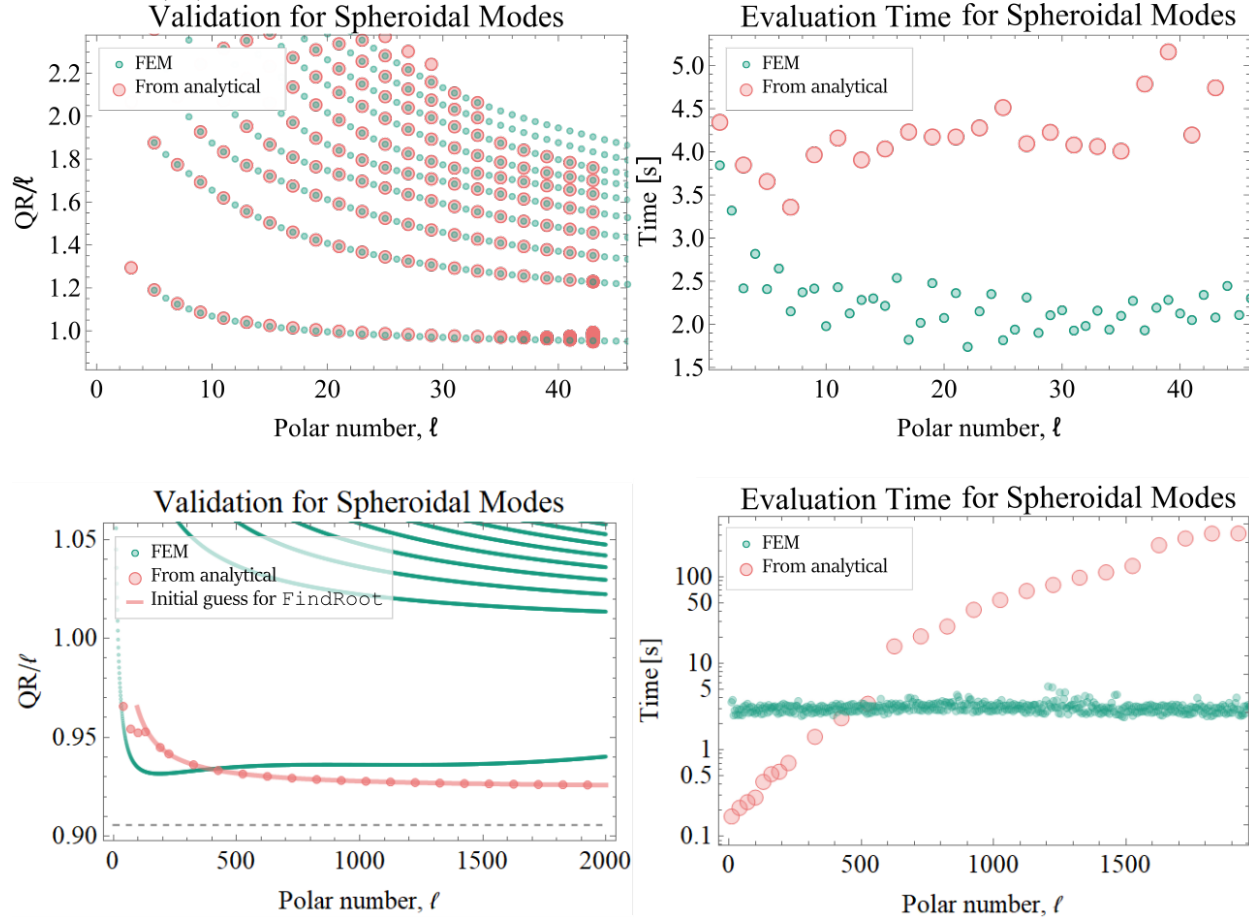


Fig. 3.8: Evaluation time comparison for spheroidal modes for a sphere with  $250\text{ }\mu\text{m}$  diameter and 50 nm alumina layer. Top Left: Validation of eigenfrequency solutions from FEM and analytical methods for small polar numbers. Top right: evaluation time comparison for low polar orders. Bottom left: attempt to extend the methods for the first mode and for large  $\ell$ , encountering precision warnings. The red curve indicates the initial guess used and we see that the method fails to converge to the FEM solutions. Bottom right: evaluation time comparison for plots on the left. We stress that the FEM times correspond to the solution of 10 modes and the analytical times correspond to the search of one root.

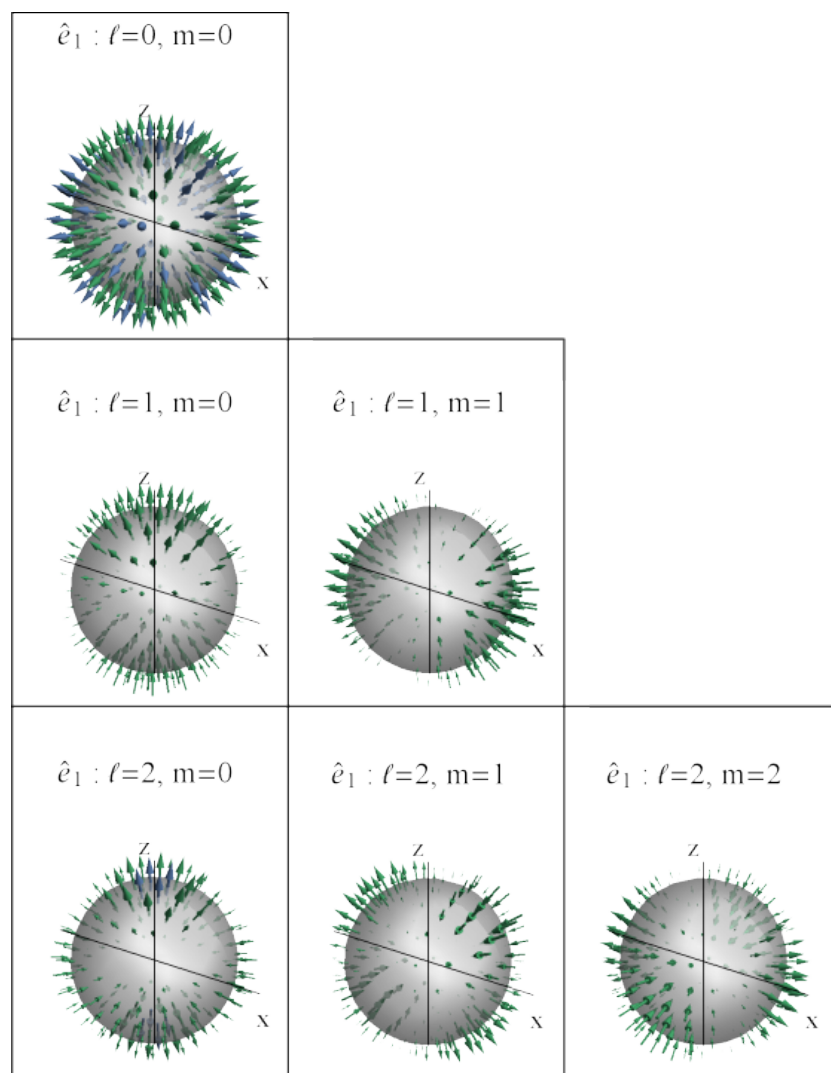
## Chapter 4

### Plan of Activities for the first semester of 2021

As mentioned in chapter 1, there are three remaining tasks for this project:

4. Implementation of faster Brillouin gain calculations based on Finite Element Method results;
5. Investigation and design of onion-like geometry responsible for giant Brillouin gain;
6. Experimental investigation of pseudo-bulk acoustic modes via Brillouin scattering interaction.

The fist two are based on simulations and the last is experimental. Task 4 is expected to be done by December 2020, and task 6 will be prioritized when the student is granted access to the laboratories at UNICAMP. Until experimental work is hindered, we will focus on task 5 redirecting the project nature: from experimental to computational.

**Appendix A****Vector Spherical Harmonics**Fig. A.1: Representation of the vector spherical harmonic  $\hat{e}_1$

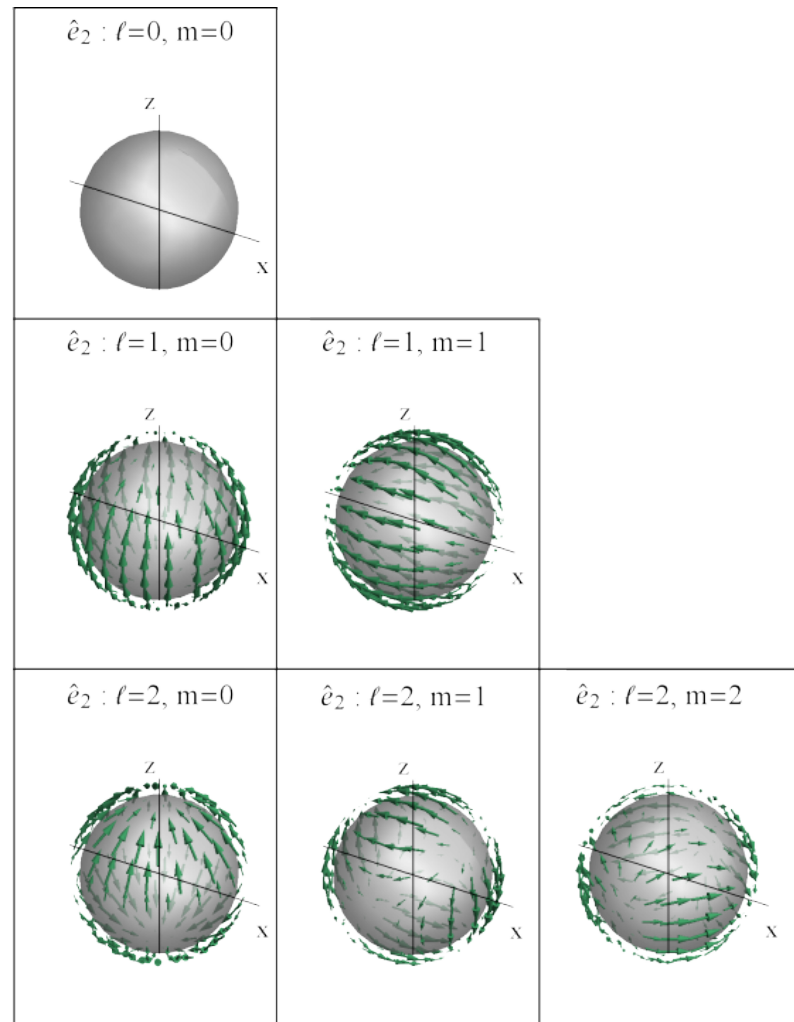


Fig. A.2: Representation of the vector spherical harmonic  $\hat{e}_2$

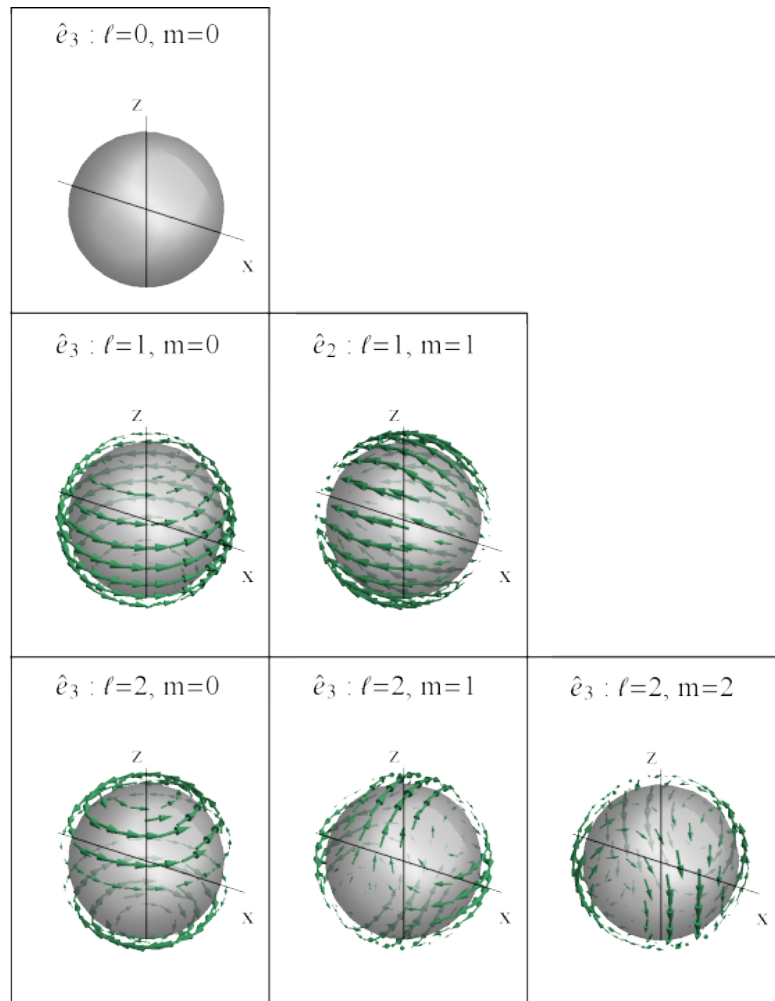


Fig. A.3: Representation of the vector spherical harmonic  $\hat{e}_3$

## Bibliography

- [1] G. P. Agrawal. *Nonlinear fiber optics*. Springer, 2000.
- [2] A. Kobyakov, et al. Stimulated brillouin scattering in optical fibers. *Advances in optics and photonics*, 2(1):1–59, 2010.
- [3] E. A. Kittlaus, et al. Large brillouin amplification in silicon. *Nature Photonics*, 10(7):463–467, 2016.
- [4] M. Merklein, et al. Enhancing and inhibiting stimulated brillouin scattering in photonic integrated circuits. *Nature communications*, 6(1):1–8, 2015.
- [5] O. Florez, et al. Brillouin scattering self-cancellation. *Nature communications*, 7(1):1–8, 2016.
- [6] H. Shin, et al. Tailorable stimulated brillouin scattering in nanoscale silicon waveguides. *Nature communications*, 4(1):1–10, 2013.
- [7] N. T. Otterstrom, et al. A silicon brillouin laser. *Science*, 360(6393):1113–1116, 2018.
- [8] K. S. Abedin, et al. Single-frequency brillouin distributed feedback fiber laser. *Optics letters*, 37(4):605–607, 2012.
- [9] S. Gundavarapu, et al. Sub-hertz fundamental linewidth photonic integrated brillouin laser. *Nature Photonics*, 13(1):60–67, 2019.
- [10] B. Vidal, et al. Tunable and reconfigurable photonic microwave filter based on stimulated brillouin scattering. *Optics letters*, 32(1):23–25, 2007.
- [11] S. Wabnitz and B. J. Eggleton. All-optical signal processing. *Data Communication and Storage Applications*, 2015.
- [12] R. Pant, et al. Photonic-chip-based tunable slow and fast light via stimulated brillouin scattering. *Optics letters*, 37(5):969–971, 2012.
- [13] J. Kim, et al. Non-reciprocal brillouin scattering induced transparency. *Nature Physics*, 11(3):275–280, 2015.
- [14] J. Li, et al. Microresonator brillouin gyroscope. *Optica*, 4(3):346–348, 2017.
- [15] N. Nishiguchi and T. Sakuma. Vibrational spectrum and specific heat of fine particles. *Solid State Communications*, 38(11):1073–1077, 1981.
- [16] H. Portales, et al. Resonant raman scattering by quadrupolar vibrations of ni-ag core-shell nanoparticles. *Physical Review B*, 65(16):165422, 2002.
- [17] U. D. Jentschura and E. Lötstedt. Numerical calculation of bessel, hankel and airy functions. *Computer Physics Communications*, 183(3):506–519, 2012.
- [18] J. Harrison. Fast and accurate bessel function computation. In *2009 19th IEEE Symposium on Computer Arithmetic*, pages 104–113. IEEE, 2009.
- [19] H. Ding, et al. *Elasticity of transversely isotropic materials*, volume 126. Springer Science & Business Media, 2006.
- [20] J.-M. Jin. *The finite element method in electromagnetics*. John Wiley & Sons, 2015.

- [21] T. I. Zohdi, et al. *A Finite Element Primer for Beginners*. Springer, 2018.
- [22] FindRoot - Wolfram Language documentation. <https://reference.wolfram.com/language/ref/FindRoot.html>. Accessed: 2020-11-27.